Biosensors and Bioelectronics 92 (2017) 724–732

Contents lists available at ScienceDirect

Biosensors and Bioelectronics

journal homepage: www.elsevier.com/locate/bios

An artemisinin-mediated ROS evolving and dual protease light-up nanocapsule for real-time imaging of lysosomal tumor cell death

Liwei Huang[b], Yingping Luo[b], Xian Sun[b], Huangxian Ju[d], Jiangwei Tian[a,b,c,*], Bo-Yang Yu[a,b,*]

[a] State Key Laboratory of Natural Medicines, China Pharmaceutical University, Nanjing 210009, PR China
[b] Jiangsu Key Laboratory of TCM Evaluation and Translational Research, Department of Complex Prescription of TCM, China Pharmaceutical University, Nanjing 211198, PR China
[c] College of Chemistry, Chemical Engineering and Materials Science, Shandong Provincial Key Laboratory of Clean Production of Fine Chemicals, Shandong Normal University, 250014, PR China
[d] State Key Laboratory of Analytical Chemistry for Life Science, School of Chemistry and Chemical Engineering, Nanjing University, Nanjing 210093, PR China

ARTICLE INFO

Keywords:
Lysosome
Tumor
Reactive oxygen species
Artemisinin
Fluorescence imaging
Nanomedicine

ABSTRACT

Lysosomes are critical organelles for cellular homeostasis and can be used as potential targets to kill tumor cells from inside. Many photo-therapeutic methods have been developed to overproduce reactive oxygen species (ROS) to trigger lysosomal membrane permeabilization (LMP)-associated cell death pathway. However, these technologies rely on extra irradiation to activate the photosensitizers, which limits the applications in treating deep seated tumors and widespread metastatic lesions. This work reports a multifunctional nanocapsule to achieve targeted lysosomal tumor cell death without irradiation and real-time monitoring of drug effect through encapsulating artemisinin and dual protease light-up nanoprobe in a folate-functionalized liposome. The nanocapsule can be specifically uptaken by tumor cells *via* folate receptor-mediated endocytosis to enter lysosomes, in which artemisinin reacts with ferrous to generate ROS for LMP-associated cell death. By virtue of confocal fluorescence imaging, the artemisinin location in lysosome, ROS-triggered LMP and ultimate cell apoptosis can be visualized with the cathepsin B and caspase-3 activatable nanoprobe. Notably, the artemisinin-mediated ROS evolving for tumor therapy and real-time therapeutic monitoring were successfully implemented by living imaging in tumor-bearing mice, which broaden the nanocapsule for *in vivo* theranostics and may offer new opportunities for precise medicine.

1. Introduction

Lysosomes are critical subcellular acidic, membrane-bound organelles for cellular homeostasis (Blott and Griffiths, 2002; Futerman and Van Meer, 2004; Stinchcombe et al., 2004). Recently, increasing evidences have shown that lysosomes become an Achilles heel of tumor cells that can trigger cell death pathway after lysosomal membrane permeabilization (LMP) (Aits and Jäättelä, 2013; Boya and Kroemer, 2008; Guicciardi et al., 2004; Gulbins and Kolesnick, 2013; Petersen et al., 2013; Saftig and Sandhoff, 2013). In the presence of appropriate stimuli such as reactive oxygen species (ROS) (Blomgran et al., 2007; Trachootham et al., 2009), lipid-mediators (Kroemer and Jäättelä, 2005; Zitvogel et al., 2010) and lysosomotropic detergents (Ostenfeld et al., 2008), lysosomes undergo membrane permeabilization, which leads to the spillage of hydrolases from lysosomal lumen into cytosol and the activation of a caspase dependent apoptosis (Johansson et al., 2010; Oberle et al., 2010). It is noteworthy that ROS-associated oxidation among these stimuli has attracted great interest because it can directly and rapidly disturb the integrity of lysosomal membrane for killing tumor cells (Denamur et al., 2011). Thus many lysosome-targeted photosensitizers have been developed to overproduce ROS under extra irradiation to damage the lysosomes (He et al., 2015; Liu et al., 2011; Mitsunaga et al., 2011; Tian et al., 2013, 2015; Wang et al., 2011a; Yuan et al., 2015). However, these photosensitizers rely on the penetration of light through tissue, making them difficult to treat deep seated tumors and widespread metastatic lesions. Therefore, new strategies that allow ROS-triggered LMP without irradiation are highly desired to increase the efficacy and practicability of current lysosome-based cancer therapeutics.

Artemisinin (ART) is a natural product isolated from the Chinese herb *Artemisia annua* L (Klayman, 1985; Miller and Su, 2011; Tu, 2011). It is a sesquiterpene lactone with an endoperoxide bridge which

---

[*] Corresponding authors at: Jiangsu Key Laboratory of TCM Evaluation and Translational Research, Department of Complex Prescription of TCM, China Pharmaceutical University, Nanjing 211198, PR China.
E-mail addresses: jwtian@cpu.edu.cn (J. Tian), boyangyu59@163.com (B.-Y. Yu).

http://dx.doi.org/10.1016/j.bios.2016.10.004
Received 12 August 2016; Received in revised form 18 September 2016; Accepted 3 October 2016

can be cleaved by Fe(II) to generate ROS (Haynes and Krishna, 2004; Liu et al., 2015; Mercer et al., 2011). Meanwhile, the content of Fe(II) in tumor cells with high proliferation is greater than that of normal cells (Daniels et al., 2006; Heath et al., 2013; Kalinowski and Richardson, 2005), thus ART offers an opportunity for ROS-triggered LMP in tumor cells without irradiation. However, some challenges are still needed to be addressed. One of the major obstacles encountered with LMP is the lack of specific delivery of hydrophobic ART into the lysosome of tumor cells (Chaturvedi et al., 2010; Jefford, 2007). Liposome, self-enclosed spheres of lipid bilayers and an aqueous core within the bilayers, can effectively improve solubility of the embedded drugs (Barenholz, 2012; Pattni et al., 2015; Torchilin, 2012). Furthermore, liposomes modified with folic acid (FA) could be employed to target tumor cells through specific binding with folate receptor (FR) that overexpressed on the membrane of tumor cells, and rapidly concentrated in the lysosomes *via* a FR-mediated endocytic pathway (Chen et al., 2013; Tian et al., 2016). We can therefore use FA modified liposome to delivery ART into the lysosomes of tumor cells.

Since lysosomes are the targeted organelles in the LMP-induced cell death, another challenge is that to develop a non-invasive imaging method to visualize the location in lysosomes, the process of LMP and the ultimate cell apoptosis, which is very important to evaluate the therapeutic efficacy. In this respect, cathepsin B (CaB) as a lysosomal cysteine protease (Mohamed and Sloane, 2006; Sevenich et al., 2010) and caspase-3 as the chief executioner in the apoptosis (Lauber et al., 2003; Shalini et al., 2015) can be used as the triggers to construct a dual-protease light-up probe for visualization. Because both of the two protease possess specific peptide cleaving capability (Lock et al., 2016;

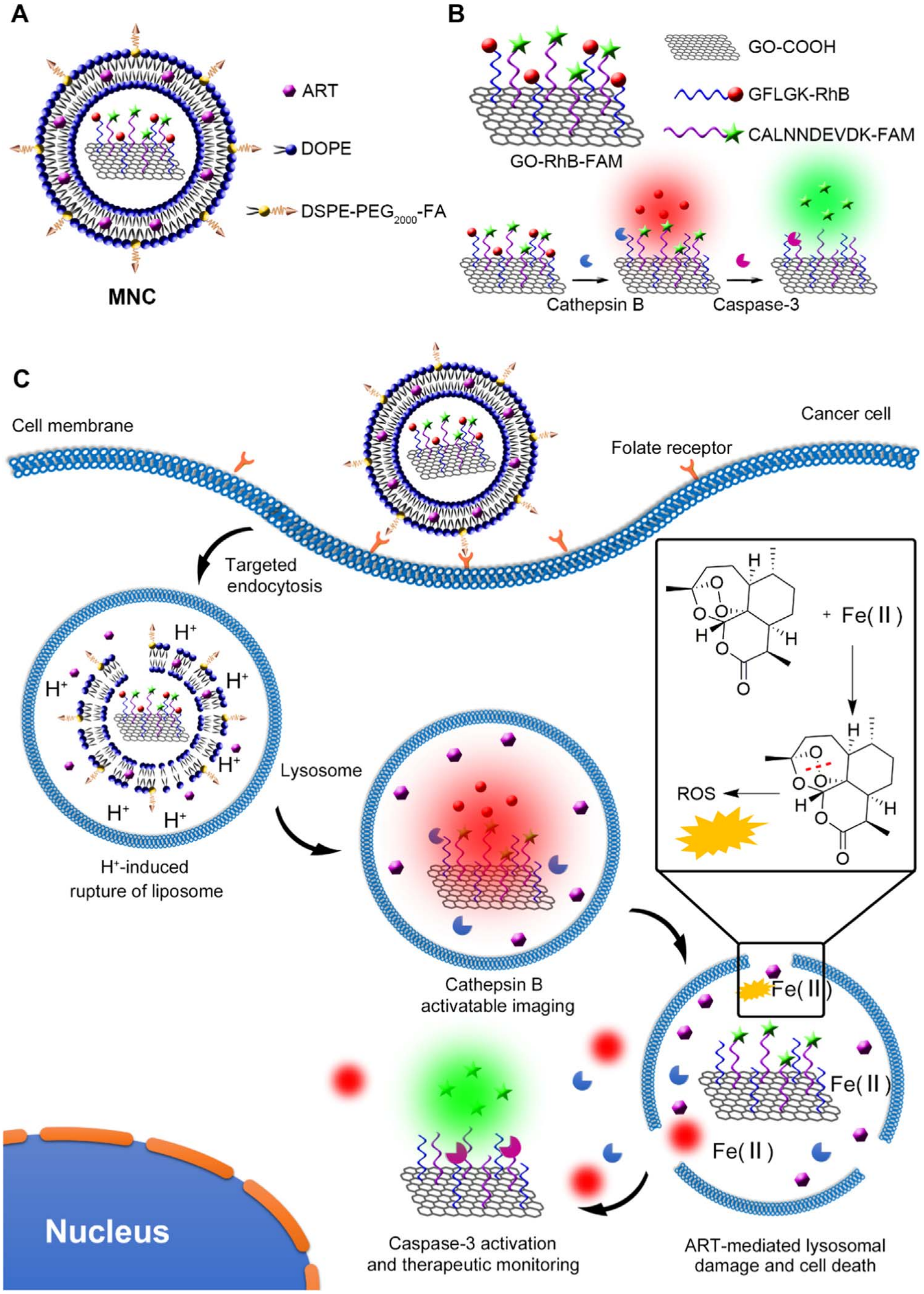

Scheme 1. Schematic illustration of (A) MNC and (B) GO-RhB-FAM for cathepsin B and caspase-3 activatable imaging and (C) FR-targeted delivery, ART-mediated ROS evolving and dual protease light-up for imaging of lysosomal tumor cell death.

Wang et al., 2011) and graphene oxide (GO) exhibits strong fluorescence quenching ability (Feng et al., 2013; Yang et al., 2013b), the conjugation of fluorophore-labeled peptides onto the surface of GO provides a convenient and feasible method for imaging the activity of CaB and caspase-3. Finally, if the dual-protease light-up nanoprobe could be integrated into the FA modified liposome loaded with ART, the theranostic efficiency will be significantly improved, and such nanomedicine has not been reported to date.

Herein, a multifunctional nanocapsule (MNC) has been designed and synthetized. It is composed by a FA modified liposome with ART encapsulated in the lipid bilayers and dual-protease light-up nanoprobe in the aqueous core (Scheme 1**A**). For real-time imaging of ART localized in lysosome and evaluation of ART-induced apoptosis, a carboxylic GO nanosheet is covalently conjugated with CaB specific substrate peptide labeled with rhodamine B (GFLGK-RhB) and caspase-3 specific substrate peptide labeled with fluorescein (CALDEVD-FAM) to act as the nanoprobe (GO-RhB-FAM). Close proximity of RhB and FAM to the GO surface results in strong inhibition of fluorescence. After the nanoprobe interacts with CaB and caspase-3, the peptide was cleaved and RhB and FAM were released from GO surface to generate fluorescence for detection of corresponding protease activity (Scheme 1**B**). The ART and GO-RhB-FAM can be integrated into the FA modified liposome by a self-assembly process to form the MNC. The MNC can be selectively taken up by FR high-expressed tumor cells into the lysosome, in which the acidic pH environment induce the rupture of liposome and the release of ART and GO-RhB-FAM. In these cases, the RhB fluorescence is recovered by CaB activation to reflect the entering of ART into the lysosome. Meanwhile, the released ART reacts with lysosomal Fe(II), leading to the breakage of endoperoxide bridge to produce ROS for LMP which can be reflected by RhB fluorescence diffusion to cytoplasm. After that, FAM fluorescence is lighten up by caspase-3 activation, providing a convenient protocol to *in situ* monitor the therapeutic efficacy (Scheme 1**C**). Therefore, this work reports a simple and effective theranostic nanomedicine for precise lysosomal cancer treatment.

2. Results and discussion

2.1. Characterization of GO-RhB-FAM

The GFLGK-RhB and CALDEVD-FAM were conjugated to carboxylic GO using the succinimide coupling (EDC-NHS) method (Sam et al., 2010; Yang et al., 2013a, 2013b). The conjugation of GFLGK-RhB and CALDEVD-FAM on GO surface was characterized by atomic force microscopy (AFM). After sonication treatment, most GO sheets showed single-layered dispersion with a dimension about 50 nm and topological height of 1.1 nm (Fig. 1**A**). After conjugation, the obtained GO-RhB-FAM nanosheets were still well dispersed and the corresponding topological height became 4.2 nm, indicating the conjugation of peptide on GO surface.

The absorption spectra of free GFLGK-RhB, CALDEVD-FAM, GO and GO-RhB-FAM nanoprobe were measured to test the conjugation of peptides on GO surface. The absorption spectrum of free GFLGK-RhB showed a peak at 566 nm with a molar absorption coefficient ε of $3.24\times10^4\ M^{-1}\ cm^{-1}$, and a strong peak at 441 nm ($\varepsilon=3.89\times10^4\ M^{-1}\ cm^{-1}$) was observed for free CALDEVD-FAM (Fig. 1**B**). The absorp-

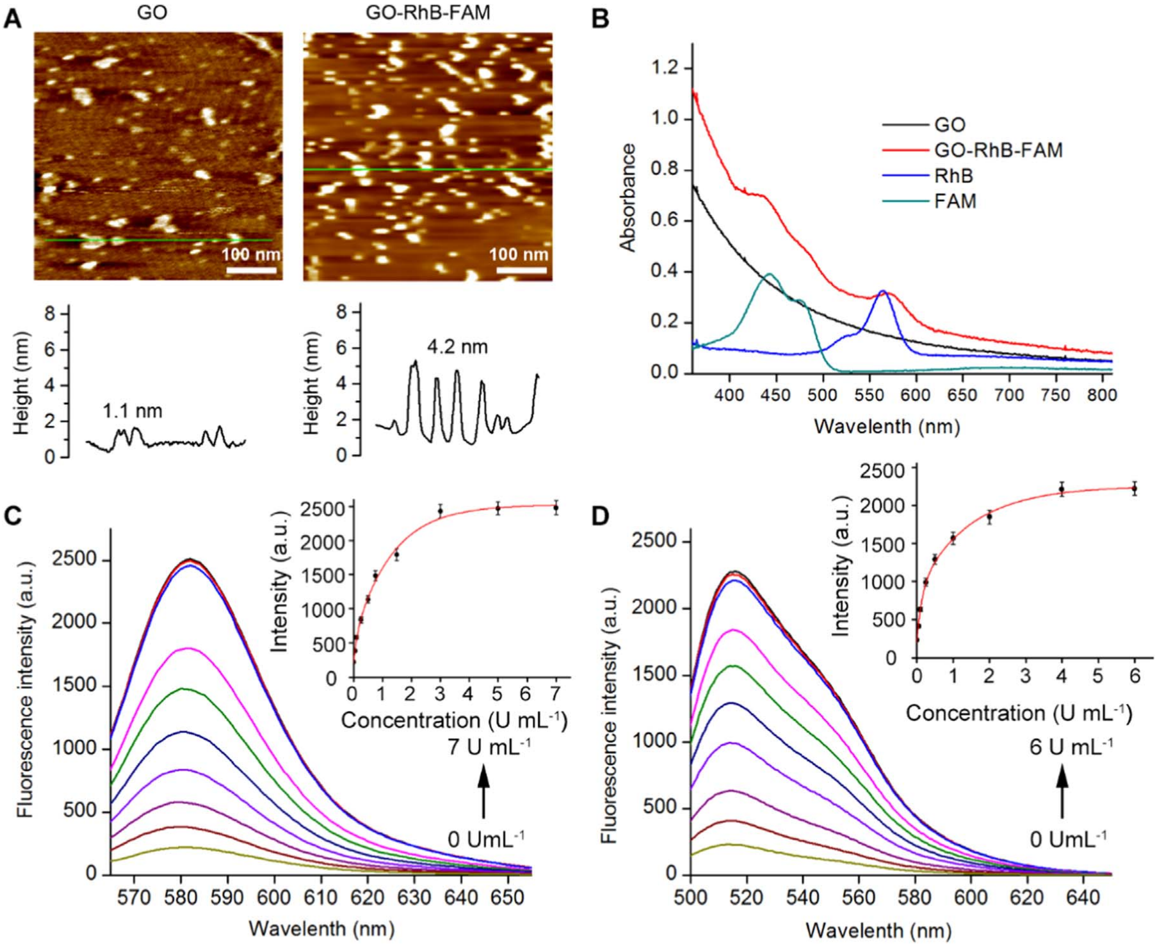

Fig. 1. (A) AFM images (top) and height profiles (bottom) of GO and GO-RhB-FAM. (B) Absorption spectral of 6.7 μM Pep-RhB, 2.5 μM Pep-FAM, 0.2 mg mL^{-1} GO and 0.2 mg mL^{-1} GO-RhB-FAM, respectively. (C) Fluorescecnce spectral and intensity at 580 nm (inset) of response of 0.2 mg mL^{-1} GO-RhB-FAM to different concentrations of CaB. (D) Fluorescecnce spectral and intensity at 520 nm (inset) response of 0.2 mg mL^{-1} GO-RhB-FAM to different concentrations of caspase-3. Data are means ± SD (n=3).

tion curve of free GO spanned over a broad range from the ultraviolet to near-infrared region. The appearance of two absorption peaks at 566 and 441 nm for GO-RhB-FAM further demonstrated the successful conjugation of GFLGK-RhB and CALDEVD-FAM on GO surface.

2.2. Fluorescence response of GO-RhB-FAM

The capabilities of the GO-RhB-FAM for *in vitro* detection of CaB and caspase-3 activity were examined with fluorescence spectra. In the absence of CaB, the fluorescence emission of GO-RhB-FAM was very weak (Fig. S1) due to the energy transfer from RhB to GO. After CaB was added into GO-RhB-FAM solution at 37 °C for 60 min, a significant fluorescence peak at 580 nm was observed, suggesting the cleavage of GFLGK and the release of RhB. On the contrary, the presence of antipain as a strong CaB inhibitor obviously hinder the fluorescence recovery of RhB after addition of CaB, which indicated the specific fluorescence response of GO-RhB-FAM to CaB. With increasing the concentration of CaB, the fluorescence intensity increased linearly over the CaB concentration range from 0.25 to 5 U mL^{-1} (Fig. 1**C**). Similarly, the GO-RhB-FAM was found to give fluorescence signals linearly correlated to the concentrations of caspse-3 range from 0.25 to 4 U mL^{-1} (Fig. 1**D**) and the specific activation of GO-RhB-FAM by caspase-3 (Fig. S2**)**. Therefore, these results demonstrated the feasibility of GO-RhB-FAM as a dual-protease light-up nanoprobe.

2.3. Characterization of MNC

Because of the hydrophobicity of ART, severe aggregation was observed in aqueous solution (Fig. S3). After encapsulation in liposome, ART was well dispersed in aqueous solution. The liposome was assembled by 1,2-distearoyl-*sn*-glycero-3-phosphoethanol-amine-*N*-[folate(poly ethylene glycol)−2000] (DSPE-PEG_{2000}-FA), 1,2-dioleoyl-*sn*-glycero-3-phosphoethanolamine (DOPE) and cholesteryl hemisuccinate (CHEMS). The ART can be embedded in the lipid bilayers through hydrophobic interaction. The encapsulation efficiency of ART in liposome was measured with UV–Vis method to be 91.7% (Fig. S4).

ART and GO-RhB-FAM were encapsulated into the liposome to construct MNC by a thin film hydration method (Chen et al., 2012; Rengan et al., 2015; Xie et al., 2012). Transmission electron microscopic (TEM) image showed well dispersed spherical structure of MNC (Fig. 2**A**), and the average size was determined to be 240 nm by dynamic light scattering (DLS) (Fig. 2**B**). The apparent zeta potential is often used as an index to reflect the stability of nanomaterials in aqueous solution (White et al., 2007). We measured the zeta potentials of MNC and MNC (without ART) as a liposome without ART encapsulation to be −26.4 ± 0.8 mV (Fig. 2**C**) and −24.7 ± 0.9 mV (Table S1), indicating the embedded ART did not influence the stability of the liposome. The zeta potential of MNC (without FA) was increased to be −15.1 ± 1.2 mV due to the lack of negatively charged FA.

GO-RhB-FAM as a hydrophilic nanoprobe was encapsulated into the aqueous core of MNC. When adding the CaB or caspase-3 into the solution of MNC, the fluorescence of RhB or FAM did not recovery, which could be explained that the membrane of liposome prevented interaction between the inside GO-RhB-FAM and outside protease. However, after Triton X-100 as a non-ionic surfactant was added into the mixture of MNC and protease, remarkable fluorescence enhancement for RhB (Fig. S5) and FAM (Fig. S6) was observed, indicating that Triton X-100 ruptured the liposome to release GO-RhB-FAM, and led to the fluorescence recovery of RhB or FAM by CaB or caspase-3 activation. A slight red-shift with about 2 nm of the fluorescence emission maxima was also observed after addition of Triton X-100, which was attributed to the disappear of confinement effect (Rainò et al. 2010) due to the shedding of RhB or FAM from the surface of GO. These results demonstrated the successful encapsulation of GO-RhB-FAM into the aqueous core of MNC.

2.4. In Vitro ART Release Profiles

The *in vitro* release of ART from MNC was investigate by equilibrium dialysis method (Modi and Anderson, 2013). At pH 7.4,

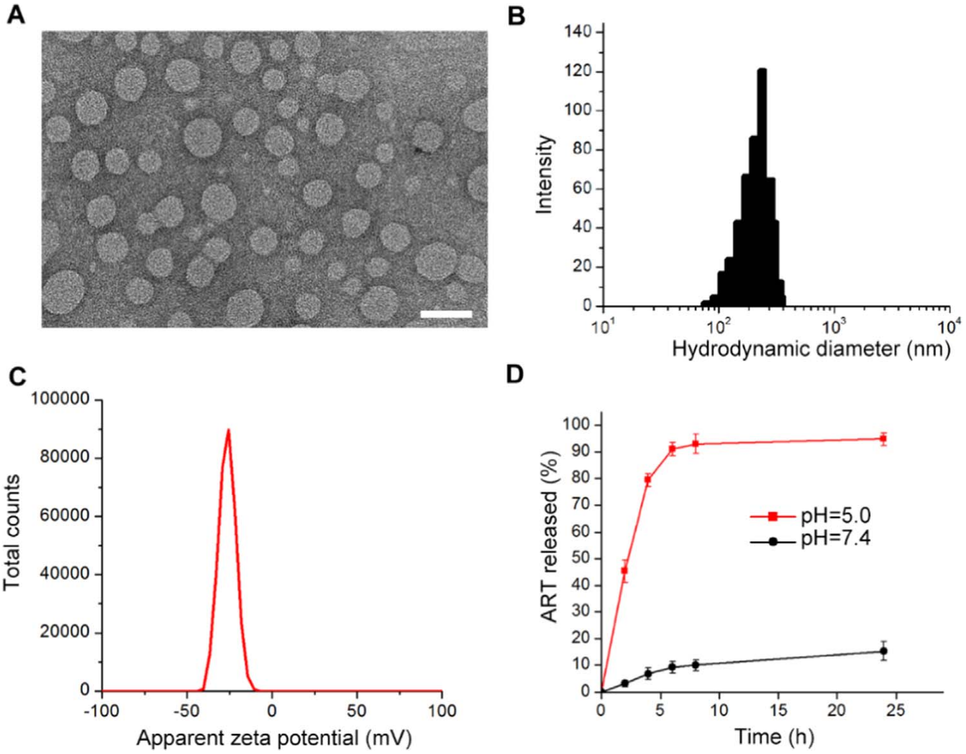

Fig. 2. (A) TEM image of MNC. Scale bar: 500 nm. (B) Size distribution of MNC measured by DLS. (C) Apparent zeta potential distribution of MNC. (D) *In vitro* release profiles of ART from MNC at pH 7.4 and 5.0. Data are means ± SD (n=3).

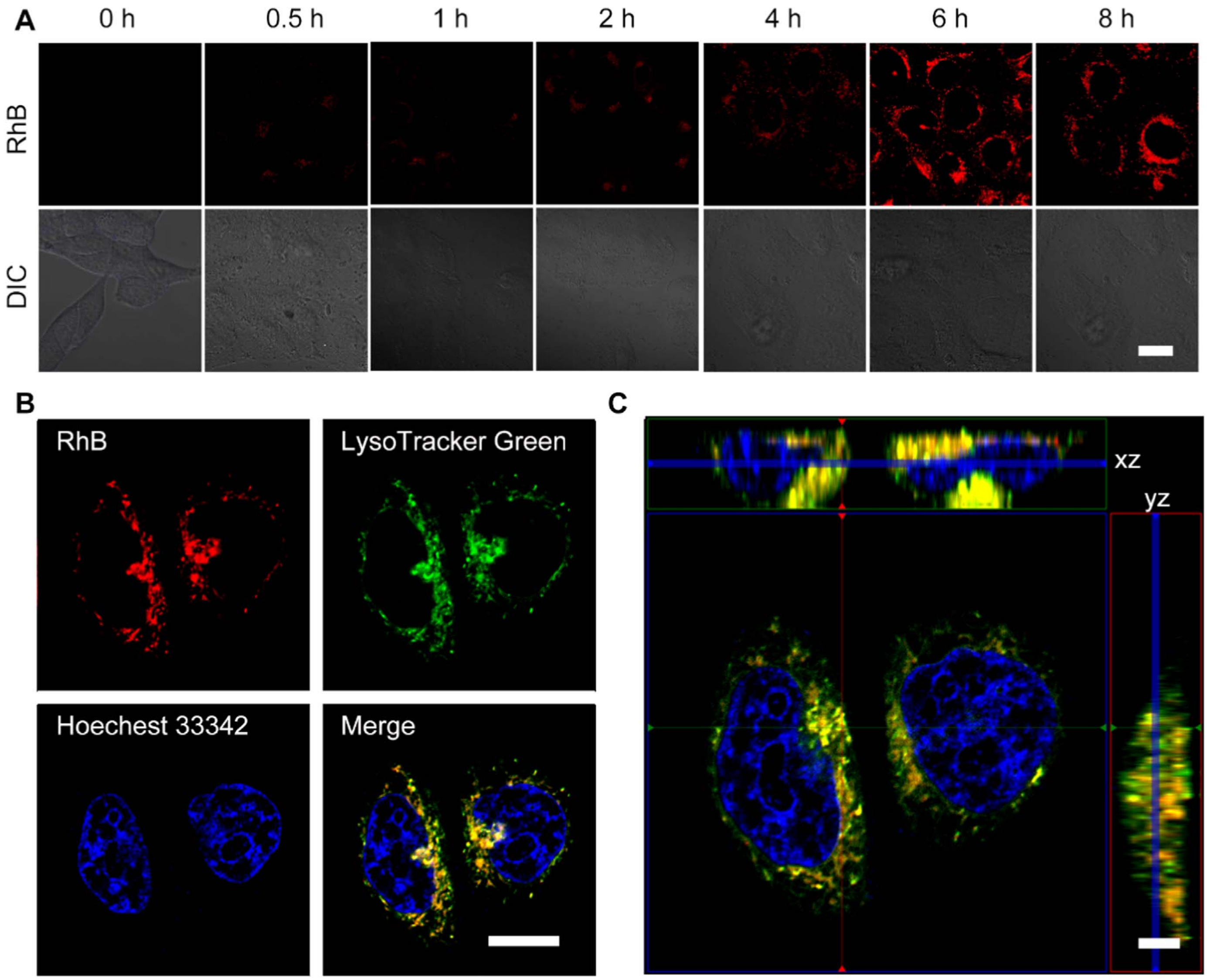

Fig. 3. Internalization and location of MNC in HeLa cells. (A) Time course fluorescence and DIC images of HeLa cells upon incubation with the MNC (6.1 μM ART equiv.). Scale bar: 25 μm. (B) Co-staining of MNC-loaded HeLa cells with LysoTracker green and Hoechst 33342. Scale bar: 15 μm. (C) Three-dimensional luminescence images of MNC-loaded HeLa cells with LysoTracker green and Hoechst 33342 (6.1 μM ART equiv.) for 6 h at 37 °C. Scale bar: 5 μm.

MNC was stable and no significant release of ART was observed over 24 h incubation (Fig. 2**D**). However, at acidic environment of pH 5.0, the ART rate of release was apparently accelerated. The accumulatively released ART could reached at 90 ± 3% after incubation for 6 h. TEM image of MNC at pH 5.0 showed cracked structures (Fig. S7), thus leading to the rapid release of ART. This pH-controllable ART release of MNC could be attributed to the presence of DOPE (Paliwal et al., 2012), a cationic lipid, which ensured an effective ART delivery and release into the acidic lysosomes of tumor cells.

2.5. Subcellular Internalization and Location of MNC

Human cervical carcinoma HeLa cells were used as a FR high-expressed cell model and incubated with MNC at 37 °C to perform confocal fluorescence imaging. After incubation for 2 h, red fluorescent spots of RhB were observed in HeLa cells (Fig. 3**A**), indicating the rapid internalization of MNC into HeLa cells and subsequently fluorescent activation by CaB. The amount and intensity of fluorescence spots increased gradually with the increasing incubation time and reached a maximum at 6 h. In order to study subcellular location of MNC in cells, the MNC-incubated HeLa cells were co-stained with a lysosome probe, LysoTracker Green, and a nucleus dye, Hoechst 33342. The red RhB fluorescence overlapped well with the green LysoTracker fluorescence (Fig. 3**B**), demonstrating that the florescence activation of the MNC occurred in lysosome. Furthermore, the stained HeLa cells was carried out by serially scanning at increasing depths along the z-axis for three-dimensional (3D) visualization. By virtue of 3D reconstruction of serial xy sections, the yellow fluorescence spots originated in fluorescent overlapping of red RhB and green LysoTracker were apparent (Fig. 3**C and Movie S1**), thus the location of MNC in lysosome could be reflected by monitoring the fluorescence of RhB.

Supplementary material related to this article can be found online at doi:10.1016/j.bios.2016.10.004.

2.6. Specificity of Internalization for MNC

To explore the targeting effect of FA, HeLa cells were also incubated with MNC (without FA). The intracellular RhB fluorescence was much weaker compared with that of MNC treated cells (Fig. S8) owing to the lack of FA targeting. As an additional control, a blocking dose of 10 μM FA was added for 30 min before the MNC incubation (FA + MNC). By observation of the intracellular RhB fluorescence, the internalization of

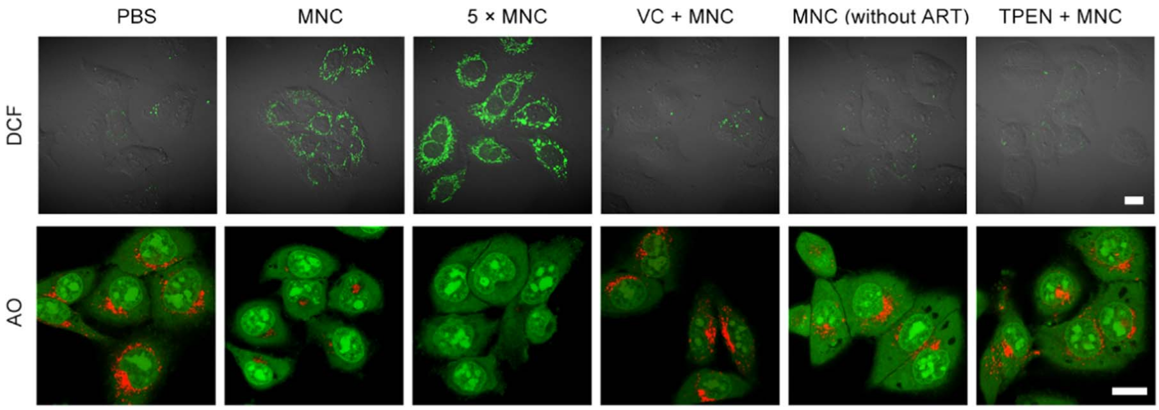

Fig. 4. Confocal fluorescent images of HeLa cells with different treatments for 6 h. The cells were treated with PBS, MNC (6.1 μM ART equiv.), MNC (30.5 μM ART equiv.), VC+MNC, MNC (without ART) or TPEN+MNC, and further incubated with DCFH-DA for 30 min or AO for 15 min before CLSM analysis. Scale bars: 20 μm.

MNC into HeLa cells was obviously suppressed, which indicated that FA played an important role in the targeted delivery of MNC into HeLa cells *via* a FR-mediated endocytosis pathway. To further investigate the specificity of internalization, FR low-expressed human lung carcinoma A549 cells were incubated with MNC for 6 h and showed much weaker signal intensity than that of FR high-expressed HeLa cells. Moreover, almost no fluorescence was observed for the MNC treated human umbilical vein endothelial HUVEC cells due to the no-expression of FR (Fig. S9). These results validated that the presence of FA on MNC specifically bound to FR that was generally overexpressed on the membrane of tumor cells, resulting in receptor-mediated endocytosis for specific imaging and drug delivery.

2.7. *Cytotoxic Selectivity of MNC*

Cytotoxicity of MNC was investigated using MTT assay. HeLa cells were incubated with various concentrations of MNC (ART equiv.) and MNC (without ART) for 24 h. The cytotoxicity increased along with the concentration of MNC (Fig. S10) with a 50% growth inhibition concentration (IC_{50}) of 6.1 μM (ART equiv.). In the absence of ART, the cell viability of the MNC (without ART) treated cells remained above 90% (Fig. S10), which indicated that the cytotoxicity of MNC was attributed to the loaded ART and the nanocapsule had good biocompatibility. Furthermore, the cytotoxicity was found to be FA dependent (Fig. S11), the cell viability of the cells treated with MNC (without FA) or FA+MNC could remain above 75%, demonstrating the necessity of FA in the targeted delivery of ART into tumor cells.

The FA-mediated targeting was further confirmed by incubating HeLa cells, A549 cells and HUVEC cells with the MNC for 24 h. Unlike HeLa cells, the cell viability remained above 75% for A549 cells and almost no cytotoxicity was observed for normal HUVEC cells (Fig. S12). Since Fe(II) is essential to induce the toxicity of ART, the intracellular content of Fe(II) was detected by an iron colorimetric assay kit. The content of Fe(II) in cancerous HeLa and A549 cells were 10-fold higher than that in normal HUVEC cells (Fig. S13), which could be ascribed to high-expressed transferrin receptors on cancer cells. Although the content of Fe(II) in A549 cells was high, the expression of FR was much lower compared with HeLa cells, leading to a lower cytotoxicity. Thus the dual targeting MNC possessed of therapeutic selectivity to FR and Fe(II) high-expressed cancer cells.

2.8. *ART-Mediated ROS Evolving and LMP*

ART-mediated ROS evolving in MNC-treated HeLa cells was evaluated with 2’,7’-dichlorodihydrofluorescein diacetate (DCFH-DA) as a ROS probe. It is non-fluorescent but can be oxidized to be highly fluorescent 2’,7’-dichlorofluorescein (DCF) by intracellular ROS (Wang et al., 2016). After staining with DCFH-DA, the MNC-treated group of HeLa cells emitted bright DCF fluorescence in lysosomes compared with that of PBS group (Fig. 4), and the fluorescence intensity was MNC concentration dependent, indicating massive production of ROS. To investigate whether the generated ROS affect the integrity of lysosome, acridine orange (AO) was employed as an indicator which emits red fluorescence in lysosomes and green fluorescence in cytosol and nuclei (Chen et al., 2014). For the MNC-treated HeLa cells, the red fluorescence from AO was remarkably decreased, demonstrating that ROS cause LMP. However, the addition of vitamin C (VC) as a ROS scavenger before MNC incubation could inhibit ROS generation, and the lysosomal compartments were well maintained. For the cells treated with MNC (without ART), or *N,N,N',N'*-tetrakis(2-pyridylmethyl)ethylenediamine (TPEN) as a high-affinity Fe(II) chelator (Jabado et al., 2003) before MNC incubation, the DCF fluorescence was significantly suppressed and the red fluorescence of AO was obvious, suggesting that ART reacts with intracellular Fe(II) to overproduce ROS in lysosome and leads to LMP.

2.9. *Therapeutic Self-monitoring*

MNC induced lysosomal tumor cell death was evaluated with confocal fluorescence imaging through monitoring RhB fluorescence diffusion and FAM fluorescence activation by caspase-3 (Fig. 5**A**). After incubation with MNC for 6 h, red RhB fluorescence was mainly concentrated in lysosomes, while no FAM fluorescence was observed. At this time point, the lysosomes were intact and the cells were healthy. However, after incubation for 12 h, red RhB fluorescence diffused to cytoplasm and green FAM fluorescence appeared, indicating the rupture of lysosomes and activation of caspase-3 in the process of apoptosis. After 24 h incubation, RhB fluorescence diffusion and FAM fluorescence activation became more apparent, demonstrating the capability of therapeutic self-monitoring.

Flow cytometry was further used to clarify the advantage of MNC for therapeutic self-evaluation (Fig. 5**B**). Without FA targeting, the nanocapsule could not be internalized into tumor cells, thus most of the cells were in the RhB^-/FAM^- region. With the help of FA targeting, the MNC (without ART) could be effectively uptaken into tumor cells as reflected by RhB fluorescence. However, without ART encapsulation, the nanocapsule did not produce ROS to induce LMP, thus most HeLa cells were located in the RhB^+/FAM^- region. For the MNC treated cells, the percentage of cells in the RhB^+/FAM^+ region significantly increased from 7.00% to 26.75%, revealing distinct cell death and self-feedback functionality for therapeutic efficacy.

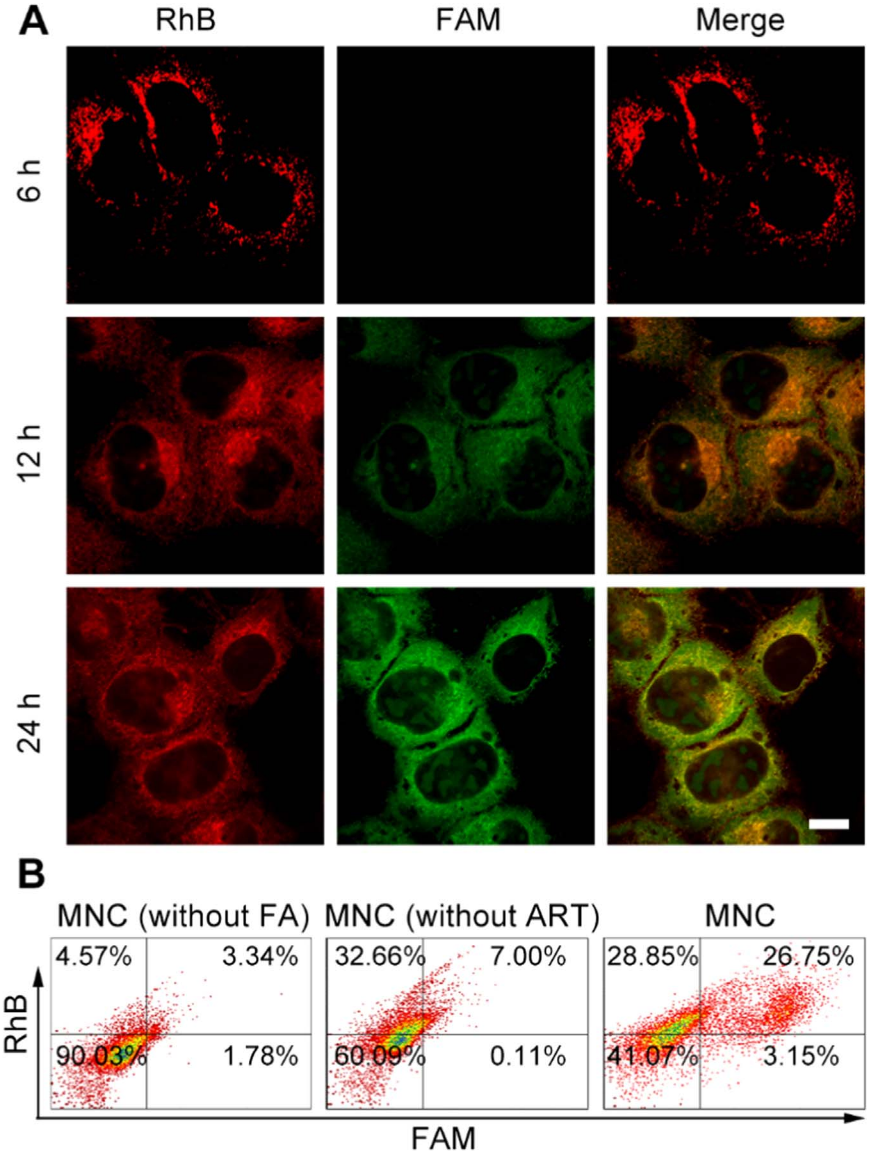

Fig. 5. (A) Time course fluorescence images of HeLa cells upon incubation with the MNC (6.1 μM ART equiv.). Scale bar: 10 μm. (B) Flow cytometer assay of HeLa cells incubated with MNC (without ART), MNC (without FA) and MCN (6.1 μM ART equiv.) for 24 h.

2.10. *In Vivo Tumor Therapy and Real-time Imaging*

HeLa tumor-bearing BALB/c nude mice were intravenously injected *via* tail vein with MNC at a dose corresponding 0.2 mg kg^{-1} of ART. After 8 h post injection, strong RhB fluorescence signal was observed from the tumor region and the signal could be sustained to be 32 h (Fig. 6**A**), validating the targeted tumor location and retention of MNC which can be selectively and effectively internalized into the lysosomes of HeLa cells to emit RhB fluorescence by CaB activation. The apoptotic FAM fluorescence signal appeared at the tumor site after 16 h post injection, revealing that tumor cells were underwent apoptosis. After 32 h post injection, the MNC-treated mice were sacrificed and the tumor and major organs were harvested for *ex vivo* imaging. Significant RhB and FAM fluorescence activation was occurred in the tumor (Fig. S14). On the contrary, the MNC (without ART) treated tumor-bearing mice showed that no FAM fluorescence signal was observed in tumor region, although the RhB fluorescence signal appeared (Fig. 6**B**). These results indicated that MNC-induced antitumor effect was attributed to ART and the therapeutic efficacy could be self-monitored in real-time.

The long term *in vivo* antitumor efficacy was further assessed by measuring the tumor volume. Tumor growth was significantly suppressed in HeLa tumor-bearing mice treated with MNC compared to the saline treated control mice (Fig. 6**C**), while no obvious therapeutic effect was observed in the MNC (without ART) treated mice, confirming the antitumor effect was attributed to ART. The HeLa tumor-bearing mice intravenously injected with MNC (without FA) showed much weaker antitumor efficiency due to the lack of FA targeting. The histologic images of the tumor section stained by hematoxylin and eosin (H & E) showed a massive tumor cell remission after treating with MNC (Fig. 6**D**). In addition, the apoptotic FAM fluorescence was also detected in the tumor slice (Fig. 6**D** and Fig. S15), providing further evidence for targeted tumor treatment and therapeutic self-evaluation. The mice were intravenously injected with different nanocapsules and the body weight during treatments was measured to assess the potential *in vivo* side effects of MNC. The mice did not show notable body weight loss during 16 days after treatment (Fig. S16). Meanwhile, no obvious pathological abnormalities were observed on major organs including heart, liver, spleen, lung and kidney for the MNC treated mice compared with other control group of mice (Fig. S17), confirming the good biosafety of MNC for *in vivo* tumor theranostics.

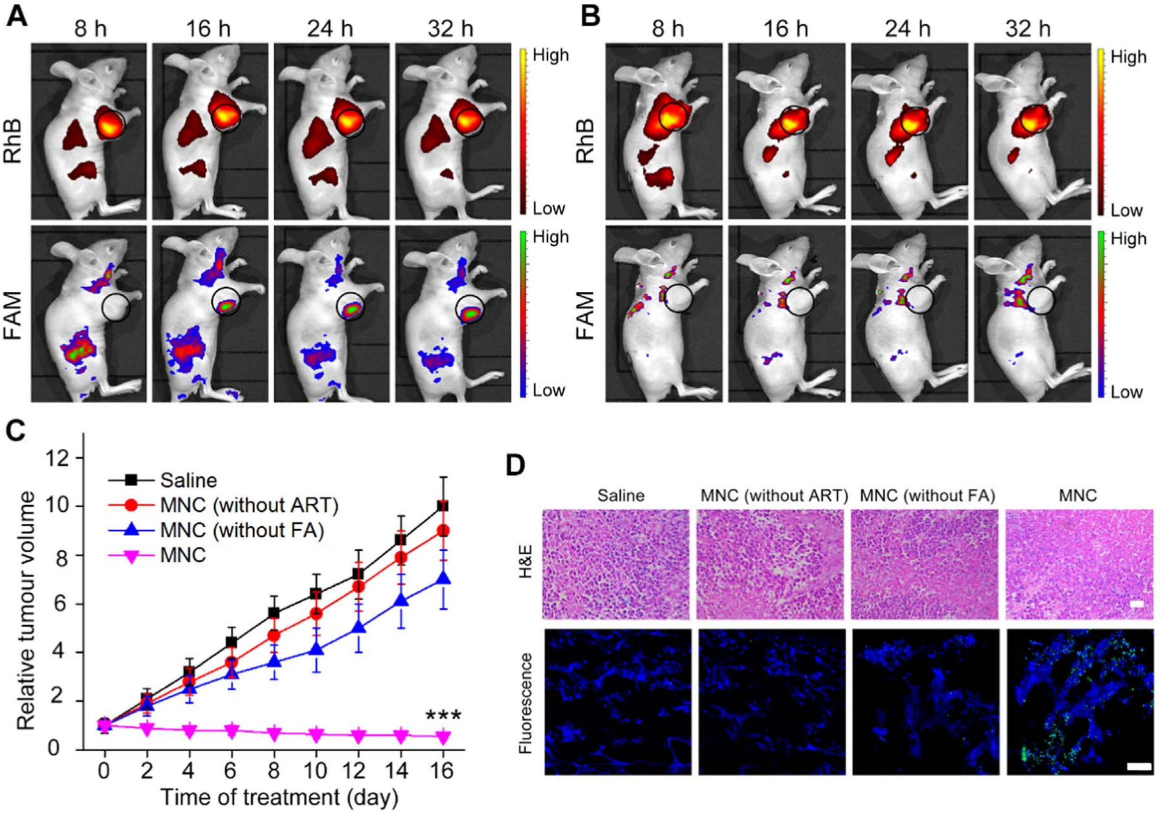

Fig. 6. *In vivo* fluorescence imaging of the HeLa tumor-bearing mice at 8, 16, 24 and 32 h after intravenous injection of (A) MNC or (B) MNC (without ART). Circle indicate the tumor region. (C) Change of relative tumor volume upon different treatments. Data are means ± SD (n=6), ***$P < 0.001$ compared to other groups using a one-way ANOVA. (D) Histological observation of the tumor tissues from different treatment groups stained with H & E and fluorescence images of tumor slice stained with Hoechst 33342. Scale bars: 100 μm.

3. Conclusions

In summary, a multifunctional nanocapsule has been developed to achieve targeted lysosomal tumor cell death and real-time therapeutic monitoring by encapsulating ART and dual-protease light-up nanoprobe into a FA-functionalized liposome. The nanocapsule with targeting properties to FR high-expressed tumor cells selectively transports and releases ART and reacts with Fe(II) to produce ROS for lysosomal damage. The fascinating advantage of the ROS-triggered lysosomal cell death strategy is its implementation without extra irradiation. By monitoring the fluorescence activation of dual-protease light-up nanoprobe, the location of ART in lysosome, the ROS-triggered LMP and the caspase-3 activation can be visualized *in situ* and in real time, which provides a valuable and convenient function for therapeutic monitoring. The nanocapsule has been successfully utilized for tumor theranostics in tumor-bearing mice and is safe for *in vivo* applications. Although autofluorescence was occurred during the *in vivo* imaging process due to the visible region of wavelength (400–700 nm), this study should substantially broaden the perspective for further manufacturing a near-infrared (700–1000 nm) nanomedicine to achieve precise tumor theranostics.

Acknowledgements

This research was supported by National Natural Science Foundation of China (21505161), Natural Science Foundation of Jiangsu Province (BK20150701), Program for Changjiang Scholars and Innovative Research Team in University (IRT1193), Shandong Provincial Key Laboratory of Clean Production of Fine Chemicals (ZDSYS-KF201503), State Key Laboratory of Analytical Chemistry for Life science (SKLACLS1415) and Graduate Student Innovation Foundation of Huahai Pharmaceutical (CX15S-005HH).

Appendix A. Supporting information

Supplementary data associated with this article can be found in the online version at doi:10.1016/j.bios.2016.10.004.

References

Aits, S., Jäättelä, M., 2013. J. Cell Sci. 126 (9), 1905–1912.
Barenholz, Y., 2012. J. Control. Release 160 (2), 117–134.
Blomgran, R., Zheng, L., Stendahl, O., 2007. J. Leukoc. Biol. 81 (5), 1213–1223.
Blott, E.J., Griffiths, G.M., 2002. Nat. Rev. Mol. Cell Biol. 3 (2), 122–131.
Boya, P., Kroemer, G., 2008. Oncogene 27 (50), 6434–6451.
Chaturvedi, D., Goswami, A., Saikia, P.P., Barua, N.C., Rao, P.G., 2010. Chem. Soc. Rev. 39 (2), 435–454.
Chen, C., Ke, J.Y., Zhou, X.E., Yi, W., Brunzelle, J.S., Li, J., Yong, E.L., Xu, H.E., Melcher, K., 2013. Nature 500 (7463), 486–489.
Chen, H.B., Xiao, L., Anraku, Y., Mi, P., Liu, X.Y., Cabral, H., Inoue, A., Nomoto, T., Kishimura, A., Nishiyama, N., Kataoka, K., 2014. J. Am. Chem. Soc. 136 (1), 157–163.
Chen, K.-J., Liang, H.-F., Chen, H.-L., Wang, Y., Cheng, P.-Y., Liu, H.-L., Xia, Y., Sung, H.-W., 2012. ACS Nano 7 (1), 438–446.
Daniels, T.R., Delgado, T., Rodriguez, J.A., Helguera, G., Penichet, M.L., 2006. Clin. Immunol. 121 (2), 144–158.
Denamur, S., Tyteca, D., Marchand-Brynaert, J., Van Bambeke, F., Tulkens, P.M., Courtoy, P.J., Mingeot-Leclercq, M.-P., 2011. Free Radic. Biol. Med. 51 (9), 1656–1665.
Feng, L., Wu, L., Qu, X., 2013. Adv. Mater. 25 (2), 168–186.
Futerman, A.H., Van Meer, G., 2004. Nat. Rev. Mol. Cell Biol. 5 (7), 554–565.
Guicciardi, M.E., Leist, M., Gores, G.J., 2004. Oncogene 23 (16), 2881–2890.
Gulbins, E., Kolesnick, R.N., 2013. Cancer Cell 24 (3), 279–281.
Haynes, R.K., Krishna, S., 2004. Microbes Infect. 6 (14), 1339–1346.
He, L., Li, Y., Tan, C.-P., Ye, R.-R., Chen, M.-H., Cao, J.-J., Ji, L.-N., Mao, Z.-W., 2015. Chem. Sci. 6 (10), 5409–5418.
Heath, J.L., Weiss, J.M., Lavau, C.P., Wechsler, D.S., 2013. Nutrients 5 (8), 2836–2859.
Jabado, N., Cuellar-Mata, P., Grinstein, S., Gros, P., 2003. Proc. Natl. Acad. Sci. U.S.A. 100(10), pp. 6127–6132.
Jefford, C.W., 2007. Drug Discov. Today 12 (11), 487–495.
Johansson, A.-C., Appelqvist, H., Nilsson, C., Kågedal, K., Roberg, K., Öllinger, K., 2010. Apoptosis 15 (5), 527–540.

Kalinowski, D.S., Richardson, D.R., 2005. Pharmacol. Rev. 57 (4), 547–583.
Klayman, D.L., 1985. Science 228 (4703), 1049–1055.
Kroemer, G., Jäättelä, M., 2005. Nat. Rev. Cancer 5 (11), 886–897.
Lauber, K., Bohn, E., Kröber, S.M., Xiao, Y.-j., Blumenthal, S.G., Lindemann, R.K., Marini, P., Wiedig, C., Zobywalski, A., Baksh, S., 2003. Cell 113 (6), 717–730.
Liu, L., Wei, Y., Zhai, S., Chen, Q., Xing, D., 2015. Biomaterials 62, 35–46.
Liu, L., Zhang, Z., Xing, D., 2011. Free Radic. Biol. Med. 51 (1), 53–68.
Lock, L.L., Reyes, C., Zhang, P., Cui, H., 2016. J. Am. Chem. Soc. 138 (10), 3533–3540.
Mercer, A.E., Copple, I.M., Maggs, J.L., O'Neill, P.M., Park, B.K., 2011. J. Biol. Chem. 286 (2), 987–996.
Miller, L.H., Su, X., 2011. Cell 146 (6), 855–858.
Mitsunaga, M., Ogawa, M., Kosaka, N., Rosenblum, L.T., Choyke, P.L., Kobayashi, H., 2011. Nat. Med. 17 (12), 1685–1691.
Modi, S., Anderson, B.D., 2013. Mol. Pharm. 10 (8), 3076–3089.
Mohamed, M.M., Sloane, B.F., 2006. Nat. Rev. Cancer 6 (10), 764–775.
Oberle, C., Huai, J., Reinheckel, T., Tacke, M., Rassner, M., Ekert, P.G., Buellesbach, J., Borner, C., 2010. Cell Death Differ. 17 (7), 1167–1178.
Ostenfeld, M.S., Høyer-Hansen, M., Bastholm, L., Fehrenbacher, N., Olsen, O.D., Groth-Pedersen, L., Puustinen, P., Kirkegaard-Sørensen, T., Nylandsted, J., Farkas, T., 2008. Autophagy 4 (4), 487–499.
Paliwal, S.R., Paliwal, R., Pal, H.C., Saxena, A.K., Sharma, P.R., Gupta, P.N., Agrawal, G.P., Vyas, S.P., 2012. Mol. Pharm. 9 (1), 176–186.
Pattni, B.S., Chupin, V.V., Torchilin, V.P., 2015. Chem. Rev. 115 (19), 10938–10966.
Petersen, N.H., Olsen, O.D., Groth-Pedersen, L., Ellegaard, A.-M., Bilgin, M., Redmer, S., Ostenfeld, M.S., Ulanet, D., Dovmark, T.H., Lønborg, A., 2013. Cancer Cell 24 (3), 379–393.
Rainò, G., Stöferle, T., Park, C., Kim, H.C., Chin, I.J., Miller, R.D., Mahrt, R.F., 2010. Adv. Mater. 22 (33), 3681–3684.
Rengan, A.K., Bukhari, A.B., Pradhan, A., Malhotra, R., Banerjee, R., Srivastava, R., De, A., 2015. Nano Lett. 15 (2), 842–848.
Saftig, P., Sandhoff, K., 2013. Nature 502 (7471), 312–313.
Sam, S., Touahir, L., Andresa, J.S., Allongue, P., Chazalviel, J.N., Gouget-Laemmel, A.C., de Villeneuve, C.H., Moraillon, A., Ozanam, F., Gabouze, N., Djebbar, S., 2010. Langmuir 26 (2), 809–814.
Sevenich, L., Schurigt, U., Sachse, K., Gajda, M., Werner, F., Müller, S., Vasiljeva, O., Schwinde, A., Klemm, N., Deussing, J., 2010. Proc. Natl. Acad. Sci. U.S.A. 107(6), pp. 2497–2502.
Shalini, S., Dorstyn, L., Dawar, S., Kumar, S., 2015. Cell Death Differ. 22 (4), 526–539.
Stinchcombe, J., Bossi, G., Griffiths, G.M., 2004. Science 305 (5680), 55–59.
Tian, J., Ding, L., Xu, H.-J., Shen, Z., Ju, H., Jia, L., Bao, L., Yu, J.-S., 2013. J. Am. Chem. Soc. 135 (50), 18850–18858.
Tian, J., Luo, Y., Huang, L., Feng, Y., Ju, H., Yu, B.-Y., 2016. Biosens. Bioelectron. 80, 519–524.
Tian, J., Zhou, J., Shen, Z., Ding, L., Yu, J.-S., Ju, H., 2015. Chem. Sci. 6 (10), 5969–5977.
Torchilin, V.P., 2012. Adv. Drug Deliv. Rev. 64, 302–315.
Trachootham, D., Alexandre, J., Huang, P., 2009. Nat. Rev. Drug Discov. 8 (7), 579–591.
Tu, Y., 2011. Nat. Med 17 (10), 1217–1220.
Wang, C., Tao, H., Cheng, L., Liu, Z., 2011a. Biomaterials 32 (26), 6145–6154.
Wang, H.B., Zhang, Q., Chu, X., Chen, T.T., Ge, J., Yu, R.Q., 2011. Angew. Chem. Int. Ed. 50 (31), 7065–7069.
Wang, T., Wang, D., Yu, H., Wang, M., Liu, J., Feng, B., Zhou, F., Yin, Q., Zhang, Z., Huang, Y., Li, Y., 2016. ACS Nano 10 (3), 3496–3508.
White, B., Banerjee, S., O'Brien, S., Turro, N.J., Herman, I.P., 2007. J. Phys. Chem. C 111 (37), 13684–13690.
Xie, R., Hong, S.L., Feng, L.S., Rong, J., Chen, X., 2012. J. Am. Chem. Soc. 134 (24), 9914–9917.
Yang, K., Feng, L., Shi, X., Liu, Z., 2013a. Chem. Soc. Rev. 42 (2), 530–547.
Yang, K., Feng, L.Z., Hong, H., Cai, W.B., Liu, Z., 2013b. Nat. Protoc. 8 (12), 2392–2403.
Yuan, Y., Zhang, C.J., Gao, M., Zhang, R., Tang, B.Z., Liu, B., 2015. Angew. Chem. Int. Ed. 54 (6), 1780–1786.
Zitvogel, L., Kepp, O., Kroemer, G., 2010. Cell 140 (6), 798–804.